

RECENT RESULTS ON DIRECT MEASUREMENT OF THE $^{12}\text{C} + ^{12}\text{C}$ FUSION CROSS SECTION AT DEEP SUB-BARRIER ENERGIES WITH STELLA*

J. NIPPERT^a, A. BONHOMME^a, S. COURTIN^{a,b}, D. CURIEN^a
E. GREGOR^a, M. HEINE^a, E. MONPRIBAT^a, T. DUMONT^a, C. STODEL^c

^aUniversité de Strasbourg, CNRS, IPHC UMR 7178, 67000 Strasbourg, France

^bUniversity of Strasbourg Institute of Advanced Studies (USIAS)
Strasbourg, France

^cGANIL, CEA/DSM-CNRS/IN2P3, Caen 14076, France

*Received 17 November 2023, accepted 5 January 2024,
published online 24 April 2024*

The measurement of $^{12}\text{C}+^{12}\text{C}$ at astrophysical energies is mandatory to well understand stellar evolution. First, fusion hindrance has been observed in most medium–heavy fusion systems, but the effect on light–medium systems is still unclear. Second, the presence of resonances in the $^{12}\text{C}+^{12}\text{C}$ fusion reaction, that can be a strong indication of molecular states in the ^{24}Mg , can also have an impact on our understanding of stellar evolution of massive stars. The precise measurements of these reaction cross sections at deep sub-barrier energies are highly challenging, as the cross section is at a sub-nanobarn level with a dominating background. To overcome this challenge, the STELLA (STELLa LABoratory) experiment combined with the UK-FATIMA (FAst TIMing Array) allows for a coincident measurement of gammas and charged particles from the fusion reaction to efficiently suppress the background and achieve precise measurements at deep sub-barriers energies in the astrophysical region of interest. The first experimental campaign in 2016/2017 revealed hints of hindrance and a potential resonance at low energies. This contribution will discuss data from the 2019 experimental campaign and give details about the experimental setup.

DOI:10.5506/APhysPolBSupp.17.3-A33

1. Introduction

The abundance of the elements around us can be tracked back to various astro-nuclear production mechanisms and sites [1] and, in fact, the synthesis of the elements and the development of the universe are mutually dependent. This comprises processes that generate the energy that stabilises stars [2] and

* Presented at the XXXVII Mazurian Lakes Conference on Physics, Piaski, Poland, 3–9 September, 2023.

that eventually drive stellar explosions leading to the injection and mixture of the generated material after the final fate of stars into space contributing to the abundance inventory around us [3], that is nowadays the main source of stellar physics knowledge. In stars, vast amounts of mostly light ionised material is gravitationally bound and heated by nuclear reactions synthesising heavier elements, and releasing typical radiation ($\alpha, \beta, \gamma, n, p \dots$). Stars heavier than $\sim 8 M_{\odot}$ [4] develop in a sequence of typical reactions where the ashes of the previous stage serve as the fuel of the subsequent burning phase. During carbon burning, two ^{12}C nuclei, that were generated before *via* the triple-alpha process [5], fuse into a highly excited compound nucleus $^{24}\text{Mg}^*$ that then mainly decays into $^{20}\text{Ne}^* + \alpha$, ($Q = 4.62$ MeV) and $^{23}\text{Na}^* + p$, ($Q = 2.24$ MeV) with subsequent emission of characteristic gammas from the de-excitation of the daughter nuclei.

The stellar fusion process takes place at temperatures of $0.8 \dots 1.5 \times 10^9$ K, which translates into relative energies of the ^{12}C nuclei far below the Coulomb barrier of the repulsive charges. Hence, the process happens *via* quantum tunneling with rapidly ceasing cross sections dropping below nanobarns in the astrophysics region of interest. Around the barrier, low lying states with reasonable overlap with the ground state can contribute to the fusion process [6, 7] opening alternative reaction channels (Q value) leading to sizeable enhancement of the cross section around a barrier distribution. The width of this distribution and the possible onset of non-coupled fusion generally affects sub-barrier cross sections [8], but is still debated for $^{12}\text{C}+^{12}\text{C}$, also due to the high energy of the first excited state.

At even lower relative energies in the deep sub-barrier energy regime, the fusion cross section was found to be suppressed in a large number of medium mass systems [8]. The impact on $^{12}\text{C}+^{12}\text{C}$ has been addressed with indirect studies as well as phenomenological models and is still debated [8, 9]. The hindrance phenomenon was attributed to the incompressibility of nuclear matter [10] or a damping of the wave function at close distances [11]. A comprehensive microscopic description is still missing and for the particular case of carbon fusion, interpretations based on the low density of states in ^{24}Mg [12] or on the Pauli principle in the compound nucleus between nucleons belonging to different nuclei leading to Pauli repulsion as the two nuclei start overlapping in the fusion process [13], are available. These Hartree-Fock calculations show no indications of fusion hindrance in $^{12}\text{C}+^{12}\text{C}$, but the authors point out the sensitivity to the sub-barrier potential and the difficulty of its reliable determination.

The $^{12}\text{C}+^{12}\text{C}$ reaction is known to reveal many resonances from energies above the barrier to deep sub-barrier energies [14, 15]. The origin of these structures is subject to long-lasting debates [16, 17] about the conditions of forming cluster and doorway states that resemble a molecule of two ^{12}C

nuclei. The discussion was revived lately with the population of possible cluster states in ^{24}Mg *via* alpha scattering, where extreme alpha branching decay ratios were measured in remarkable agreement with first principle calculations [18, 19].

The discovery of fusion hindrance intensified once more the efforts to precisely determine the fusion cross sections of $^{12}\text{C}+^{12}\text{C}$ with recent sophisticated direct and indirect measurements [15, 20–23]. In the following, the gamma-particle coincidence experiments with nanoseconds timing with STELLA are described in more detail.

2. Experimental setup

The mobile measurement station is designed for detecting light charged particles and de-excitation gammas from reactions at the deep Coulomb barrier energy and is described in more detail in [24]. The sampling periods of the STELLA and FATIMA digitizers allow for unambiguous separation of protons and alphas with nanoseconds timing gates on the coincidences. This enables surpassing background suppression resulting in ultra clean detection of fusion cross sections below nanobarn. Online monitoring and offline analysis routines are established to guarantee reliable measurements during weeks of data taking. To withstand μA beam intensity, the apparatus is equipped with a rotating target mechanism for efficient heat dissipation in the thin target foils.

The present carbon fusion experiment was carried out at the Andromède accelerator at IJCLab, Orsay (France) with $^{12}\text{C}^{2,3+}$ beams with an intensity of up to $5 \mu\text{A}$ on thin carbon target foils of $30 \dots 50 \mu\text{g}/\text{cm}^2$. The scattering chamber was equipped with two Micron S3 type detectors covering lab system polar angles $10^\circ \dots 30^\circ$ (S3F) and $148^\circ \dots 168^\circ$ (S3B). The gamma detection was carried out with 34 $\text{LaBr}_3(\text{Ce})$ detectors from the UK-FATIMA Collaboration [25, 26].

2.1. Target thickness and composition

A target foil with a 5 cm diameter frame is shown in Fig. 1. The beam impinges at an outer radius and the rotation under the beam spot forms a track from heating. The material was analysed with the Raman spectroscopy and no significant change in the morphology (disordered and amorphous carbon) was detected (see [22] for details). In order to prevent carbon buildup [27, 28], the measurements were carried out in ultra-high vacuum (10^{-8} mbar) avoiding outgassing materials inside the chamber or from pumping, while the impinging beam was moderately heating the target. They were systematically characterised after fabrication at GANIL, France, by high-precision weighting, monitored during the experiment by

means of the counting rate ratio of elastically scattered carbon beam, and evaluated after the experiment by scanning with a collimated ^{241}Am source comparing the radiated and non-radiated area.

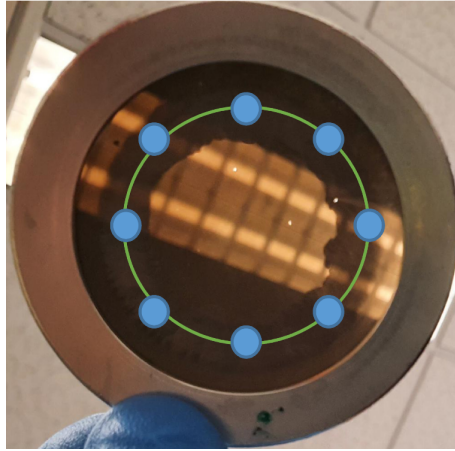


Fig. 1. (Colour on-line) Carbon target foil ($\sim 30 \mu\text{g}/\text{cm}^2$) with a track from irradiation with carbon beam (beam spot diameter $\sim 0.6 \text{ cm}$). The blue/light grey markers indicate the ^{241}Am measurements iterated with the central (non-irradiated) position.

A typical alpha source scan along eight positions is presented in Fig. 2, where positions 1 and 9 are identical and repeated to check the consistency of the approach. Data were fit by a periodic function (in red solid) reflecting

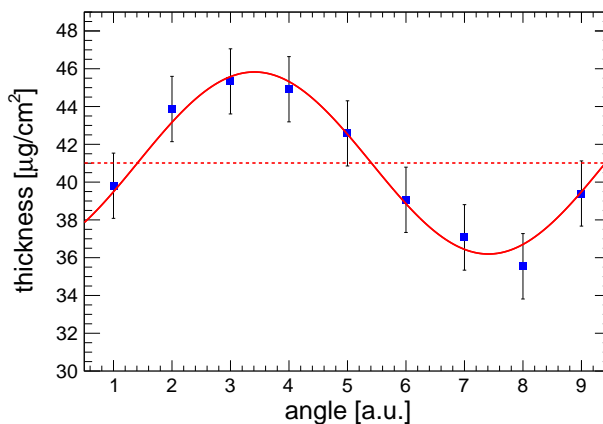


Fig. 2. (Colour on-line) Target thickness scan as a function of the position, where position 1 and 9 are identical measurements and repeated. The red solid curve represents a fit, the red dashed curve is the average thickness from the fit.

the fact that the target foil sheet has a thickness gradient with constant thickness perpendicular to the direction of thickening. The fact is illustrated in Fig. 3 in Cartesian coordinates with a target thickness gradient of about $2.9(5) \mu\text{g}/\text{cm}$, taken from the linear fit. The effect might be linked to the fabricating of the extended carbon foil sheet with the gradient reflecting the geometry of the carbon vapour chamber as well as a vapour deposition efficiency variation along the (rectangular) polarised purging elements. In the frame of this work, multiple targets were analysed with gradients between $0.9(9) \mu\text{g}/\text{cm}$ and $6.6(9) \mu\text{g}/\text{cm}$. An extended carbon foil can be used for six rotating target foils and targets can be tracked back to the production foil with the gradient.

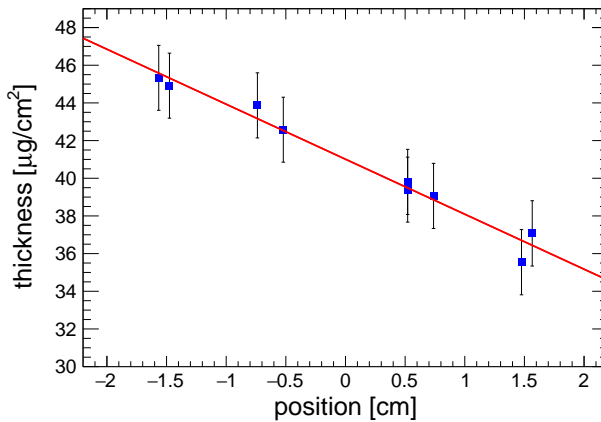


Fig. 3. (Colour on-line) Target thickness gradient in Cartesian coordinates with a linear fit (red).

The ^{241}Am source measurement complements the monitoring of the target thickness before, during, and after the experiment and, moreover, improves the uncertainty to $\leq 10\%$ by comparing the average thickness (red dashed curve in Fig. 2) to the weight after production. During the experiment, only the average value enters as the target rotates.

3. Experimental results and discussion

During the present carbon fusion experiment, the sub-barrier energy regime E_{rel} from 3.1 to 3.5 MeV was scanned at six different energies (High Energy Region HER) and one measurement was carried out at $E_{\text{rel}} = 2.4$ MeV (Low Energy Region LER). In addition, supplementary fusion data to compare with previously examined (higher) energies was analysed in order to guarantee the accuracy of the work presented here.

Such a measurement of the angular differential cross section is displayed in Fig. 4 for $^{12}\text{C}+^{12}\text{C}$ with alpha emission to the ground state of ^{20}Ne . Data from S3F and S3B in red are mirrored around 90° in grey to guide the eye and to check consistency. The measurements were fit with Legendre polynomials up to order six (upper blue/black) and eight (lower red/grey). The residue in the lower panel follows the same colour coding and reveals higher consistency of the Legendre polynomials of the order of six. Note that each measurement/strip was normalised to the respective solid angle, target thickness, and beam exposure. The associated uncertainty also includes the present geometrical systematics relevant for the boost into the centre-of-mass system. The cross section is then extracted from the associated Legendre polynomial of the order of zero and is consistent with previous findings, but allows for measurements with higher precision of 16% (systematic and statistic). The leading Legendre polynomial to a final state reveals the angular momentum carried by the light evaporated particle and a comprehensive analysis allows for the determination of the spin parity state in the compound nucleus ^{24}Mg . For this purpose, a detector was placed at steep angles $\sim 60^\circ \dots 90^\circ$, where visible information is currently missing. The addition of this detector will facilitate a clear identification of the leading Legendre polynomial, *i.e.* distinguishing unambiguously between order six and order eight in Fig. 4.

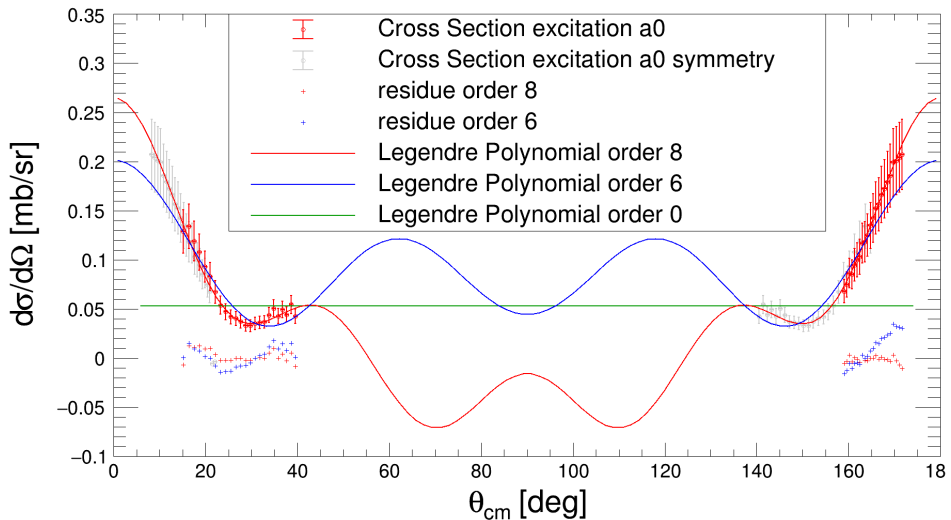


Fig. 4. (Colour on-line) Angular differential fusion cross section for the population of the ground state in ^{20}Ne versus c.m.s. polar angle at $E_{\text{rel}} = 5.5$ MeV. Data of S3F and S3B in red are mirrored in grey around the symmetry axis of 90° to guide the eye. The Legendre polynomial of order zero (horizontal green/light grey), six (upper blue/black), and eight (lower red/grey) are displayed. The lower panel contains the residue with respect to the colour-coded fit function [29].

The angular distributions in the HER were systematically analysed for the publication of Fruet *et al.* [22] with the present experimental setup. Towards the LER, the angular distributions cease with only low angular momentum of the evaporated particle (see also [30, 31]), and the geometrical mean was taken for the cross-section calculation. The inflicted error is smaller than the statistical uncertainty in the LER.

The cross sections are then expressed in terms of the modified S -factor $S^* = \sigma E \exp(2\pi\eta + gE)$ to compensate for the tunnelling through the Coulomb barrier, where $\eta = Z_1 Z_2 e^2 / \hbar v$ denotes the Sommerfeld parameter and the $g = 0.122 \sqrt{\mu R^3 / Z_1 Z_2}$ is a simple form factor in $^{12}\text{C} + ^{12}\text{C}$ reactions, with reduced mass μ , the square-well radius R , and the charge $Z_{1,2}$ of the nuclei. The correction $\exp(gE)$ is a form factor and is needed for the large interaction radius and energy involved. The HER measurements are motivated by significant discrepancies between comprehensive earlier campaigns that start emerging [15, 30]. Our data in the proton channel are in general agreement with Spillane *et al.* [15], but with drastically reduced uncertainty, identifying a significant drop of the S^* -factor. Some data points of the alpha channel in the HER deviate from [15] by up to $\sim 60\%$, but the S^* -factor appears flat and no drastic drop is detected. The energy in the LER was chosen between two previous coincidence measurements, where partly only limits exist, but no data points [22]. The cross-section data points are below nanobarn with statistical uncertainties of 70% for alphas and 82% for protons. The current measurement favours the interpretation of the S^* -factor trend given by Fruet *et al.* [22].

We thank G. Frémont (GANIL, Caen, France) for the excellent preparation of the reaction targets. The construction of STELLA was funded by the University of Strasbourg IdEX program and CNRS Strasbourg. The Andromède facility (ANR-10-EQPX-23) was funded by the program for future investment, EQUIPEX. J.N. acknowledges support from the Interdisciplinary Thematic Institute QMat, as a part of the ITI 2021–2028 program of the University of Strasbourg, CNRS and Inserm, which was supported by IdEx Unistra (ANR 10 IDEX 0002), and by SFRI STRAT'US project (ANR 20 SFRI 0012) and EUOQMAT ANR-17-EURE-0024 under the framework of the French Investments for the Future Program. S.C. acknowledges support from their Fellowships in the University of Strasbourg Institute of Advanced Study (USIAS). T.D. is supported by the European Union (ChETEC-INFRA, project No. 101008324)

REFERENCES

- [1] E. Burbidge, G. Burbidge, A. Fowler, F. Hoyle, *Rev. Mod. Phys.* **29**, 547 (1957).
- [2] M. Schwarzschild, «Structure and Evolution of the Stars», *Princeton Univ. Press*, 1958.
- [3] K. Lodders, *Astrophys. J.* **591**, 1220 (2003).
- [4] L. Siess, *Astron. Astrophys.* **448**, 717 (2006).
- [5] F. Hoyle, *Astrophys. J. Suppl.* **1**, 121 (1954).
- [6] B.B. Back *et al.*, *Rev. Mod. Phys.* **86**, 317 (2014).
- [7] G. Montagnoli, A. Stefanini, *Eur. Phys. J. A* **59**, 138 (2023).
- [8] C.L. Jiang *et al.*, *Eur. Phys. J. A* **57**, 235 (2021).
- [9] N.T. Zhang *et al.*, *Phys. Lett. B* **801**, 135170 (2020).
- [10] Ş. Mişicu, H. Esbensen, *Phys. Rev. Lett.* **96**, 112701 (2006).
- [11] T. Ichikawa, K. Hagino, A. Iwamoto, *Phys. Rev. C* **75**, 057603 (2007).
- [12] C.L. Jiang *et al.*, *Phys. Rev. Lett.* **110**, 072701 (2013).
- [13] K. Godbey, C. Simenel, A.S. Umar, *Phys. Rev. C* **100**, 024619 (2019).
- [14] E. Almqvist, D.A. Bromley, J.A. Kuehner, *Phys. Rev. Lett.* **4**, 515 (1960).
- [15] T. Spillane *et al.*, *Phys. Rev. Lett.* **98**, 122501 (2007).
- [16] E. Vogt, H. McManus, *Phys. Rev. Lett.* **4**, 518 (1960).
- [17] P. Taras, *AIP Conf. Proc.* **47**, 234 (1978).
- [18] P. Adsley *et al.*, *Phys. Rev. Lett.* **129**, 102701 (2022).
- [19] Y. Chiba, M. Kimura, *Phys. Rev. C* **91**, 061302(R) (2015).
- [20] C.L. Jiang *et al.*, *Nucl. Instrum. Methods Phys. Res. A* **682**, 12 (2012).
- [21] A. Tumino *et al.*, *Nature* **557**, 687 (2018).
- [22] G. Fruet *et al.*, *Phys. Rev. Lett.* **124**, 192701 (2020).
- [23] W.P. Tan *et al.*, *Phys. Rev. Lett.* **124**, 192702 (2020).
- [24] M. Heine *et al.*, *Nucl. Instrum. Methods Phys. Res. A* **903**, 1 (2018).
- [25] O.J. Roberts *et al.*, *Nucl. Instrum. Methods Phys. Res. A* **748**, 91 (2014).
- [26] M. Rudigier *et al.*, *Nucl. Instrum. Methods Phys. Res. A* **969**, 163967 (2020).
- [27] M.J.F. Healy, *Nucl. Instrum. Methods Phys. Res. B* **129**, 130 (1997).
- [28] E.F. Aguilera *et al.*, *Nucl. Instrum. Methods Phys. Res. B* **244**, 427 (2006).
- [29] J. Nippert, Ph.D. Thesis, University of Strasbourg, France, 2023.
- [30] H.W. Becker *et al.*, *Z. Physik A* **303**, 305 (1981).
- [31] M.G. Mazarakis, W.E. Stephens, *Phys. Rev. C* **7**, 1280 (1973).